Acta Materialia 286 (2025) 120711

Contents lists available at ScienceDirect

Acta Materialia

journal homepage: www.elsevier.com/locate/actamat

Full length article

Anisotropic structure in a vapor-deposited Pd-based metallic glass

Peihao Sun [a,*], Alessandro Martinelli [a,b], Jacopo Baglioni [a], Francesco Dallari [a], Marco Di Michiel [c], Alexey P. Melnikov [c], Konrad Samwer [e], J.B. Hastings [d], Giulio Monaco [a]

[a] Dipartimento di Fisica e Astronomia "Galileo Galilei", Università degli Studi di Padova, Via F. Marzolo, 8, Padova, 35131, PD, Italy
[b] Laboratoire Charles Coulomb, Université de Montpellier, CNRS, Montpellier, 34095, France
[c] ESRF, The European Synchrotron, 71 Avenue des Martyrs, CS40220, Grenoble, 38043 Cedex 9, France
[d] SLAC National Accelerator Laboratory, 2575 Sand Hill Rd, Menlo Park, 94025, CA, USA
[e] I. Physikalisches Institut, University of Goettingen, Goettingen, 37077, Germany

ARTICLE INFO

Keywords:
Metallic glass
Ordering
X-ray total scattering
Physical vapor deposition
X-ray nanofocus

ABSTRACT

The understanding of the structure of amorphous solids beyond nearest-neighbors has long been sought after. While recent works have demonstrated evidence for medium-range ordering and its importance for the physical properties of glassy systems, few have investigated mesoscopic structural correlations beyond a few nanometers. In this work, combining X-ray nano-diffraction with high-energy X-ray total scattering with a small focus, we have not only found structural anisotropy in a vapor-deposited $Pd_{77.5}Cu_6Si_{16.5}$ metallic glass sample which appears to show two distinct and well-defined structures in different directions, but also obtained detailed characterizations of this anisotropic structure in real space. Upon annealing, the sample loses the long-range anisotropy, and at the same time, it appears to densify with a contraction of higher-order coordination shells. In light of recent works, our results may indicate a transition between two structures in the sample with different densities, medium-range ordering, and degrees of anisotropy. We expect these results to be relevant to a larger family of metallic glass systems, where similar discoveries may be made with the use of high-quality, small-focus X-ray beams.

1. Introduction

The structure of amorphous materials continues to be a topic of interest. While short-range ordering (SRO) manifesting itself as well-defined coordination shells in density-density correlation functions has long been observed in liquids and glasses, the structure beyond SRO has traditionally been assumed to be random. In recent years, evidence has begun to emerge for structural ordering at length scales much beyond the first few atomic shells [1,2], possibly up to 5–6 nanometers and above [3]. Nonetheless, it remained unclear if long-range structural correlations can exist in amorphous materials. This is at least partly due to the non-crystalline nature of these systems, which makes it difficult to identify any kind of symmetry breaking in direct structural characterizations. Some earlier works have found magnetic anisotropy in vapor-deposited Tb-Fe films and related structural anisotropy between in-plane and out-of-plane directions [4–7]. Indirect evidence for long-range structural correlations has also been found in a $Ce_{75}Al_{25}$ metallic glass, in which different sections, even centimeters apart, appeared to share the same crystalline orientation when devitrified under pressure [8].

In a previous work [9], we have reported, to our knowledge, the first observation of local mesoscale structural correlations in a vapor-deposited $Pd_{77.5}Cu_6Si_{16.5}$ metallic glass sample. These structural correlations show up as anisotropy in the X-ray diffraction patterns whose direction changes depending on the position on the sample, with a correlation length on the order of one to a few hundred nanometers. Upon annealing, the anisotropy disappears beyond detectable levels. Our data allow us to exclude alternative explanations, leading to the conclusion that the anisotropy must be intrinsic to the structure of the sample. The results provide direct evidence that correlations can exist even on the mesoscopic scale (100 nm or above) in an otherwise completely amorphous metallic glass sample, calling for a reconsideration of the structure of disordered materials in general.

Of particular note is the use of a high-quality X-ray beam with a small focus on the scale of 100 nm and below. This, combined with the utilization of 2D X-ray detectors, made it possible to observe and

* Corresponding author.
E-mail address: peihao.sun@unipd.it (P. Sun).

https://doi.org/10.1016/j.actamat.2025.120711
Received 30 July 2024; Received in revised form 18 December 2024; Accepted 2 January 2025
Available online 8 January 2025
1359-6454/© 2025 The Authors. Published by Elsevier Inc. on behalf of Acta Materialia Inc. This is an open access article under the CC BY-NC-ND license (http://creativecommons.org/licenses/by-nc-nd/4.0/).

quantify local anisotropy which would have been very difficult to detect previously.

Nevertheless, the details of the anisotropic structure and its evolution upon annealing remain to be determined. To achieve this would require a high-energy X-ray beam with a sufficiently small focus, which has become a reality recently [10]. Taking advantage of this new possibility, we perform X-ray total scattering measurements on the anisotropic sample. Our results, combined with the X-ray nano-diffraction data, allow us to examine the details of the anisotropic structure in real space and its changes upon annealing. We further characterize the thermodynamic properties of the sample with fast differential scanning calorimetry measurements. We discuss the significance of our observations for the understanding of metallic glass structures as well as the possible thermodynamic scenarios behind the structural transformations.

2. Experimental

The samples are $Pd_{77.5}Cu_6Si_{16.5}$ (at.%) metallic glasses which are vapor-deposited onto a polished single-crystal NaCl substrate at a deposition rate of 1 nm/s and with the substrate temperature kept around $0.80T_g$ to $0.85T_g$. The deposited sample thickness is about 5 μm. More details about the sample preparation method are provided in Ref. [11].

The X-ray nano-diffraction experiment was carried out at beamline ID13 of ESRF - The European Synchrotron. The X-ray photon energy was 13 keV. The full width at half maximum (FWHM) at the sample position was estimated to be around 60 nm × 60 nm using a 2D transmission scan on a high-resolution X-ray chart. The diffraction patterns were collected by an EIGER 4M detector (DECTRIS, Baden-Dättwill, Switzerland) placed 70 mm behind the sample, perpendicular to and centered around the X-ray beam. We typically took 2D raster scans with step sizes of at least 100 nm. Further details are provided in Ref. [9]. Note that we have confirmed the absence of X-ray radiation effects in our previous work [9].

The high-energy X-ray diffraction measurements were carried out at beamline ID15A of ESRF [10]. The diffraction patterns were collected by a Pilatus3 X CdTe 2M area detector (DECTRIS) which was placed 231 mm behind the sample, perpendicular to and centered around the X-ray beam. The X-ray photon energy was 69 keV. The X-ray beam was focused by a pair of Kirkpatrick-Baez multilayer mirrors. The FWHM of the focused beam was determined to be approximately 300 nm × 450 nm, obtained by scanning a Au single crystal (dimensions smaller than 100 nm) across the focal spot and collecting the diffraction signal with the area detector.

For simplicity and clarity, in the following text, we refer to the data collected at ID13 using the nano-focused 13 keV beam as "nano-diffraction data", and to the data at ID15A using the 69 keV beam as "total scattering data".

The energy dispersive X-ray spectroscopy (EDX) measurements were performed at 15 keV electron energy with a Zeiss SIGMA HD field-emission scanning electron microscope (SEM) equipped with an Oxford Instrument EDX detector.

The fast differential scanning calorimetry (FDSC) measurements were carried out using a commercial Flash DSC 2+ machine (Mettler Toledo, Greifensee, Switzerland). Small pieces are cut from the sample and placed at the center of a standard UFS 1 sensor (Mettler Toledo). Because the active area of the chip is of size 250 μm × 250 μm, the lateral dimension of the sample pieces is typically on the order of 50-100 μm. The thickness, on the other hand, is that of the original sample, about 5 μm. The sample mass is thus on the order of a few hundred nanograms. For comparison, we have also measured pieces from a ribbon sample produced by melt-spinning with the same nominal composition, $Pd_{77.5}Cu_6Si_{16.5}$. The thickness of this ribbon sample is around 45 μm.

3. Results

3.1. Bimodal distribution of the anisotropic structure

We begin by examining details of the nano-diffraction data, which consists of 31 × 31 images in a 2D raster scan with 100 nm step size. The data is analyzed following a similar procedure as in our previous work [9]: First, we subtract the air scattering background and normalize the image by the total intensity around the first diffraction ring. Using $I_j(\mathbf{Q})$ to denote the jth image from the scan after the background subtraction and normalization, where $\mathbf{Q}$ is the momentum transfer corresponding to each pixel, we define the processed images $\delta I_j(\mathbf{Q})$ as:

$$\delta I_j(\mathbf{Q}) = \frac{I_j(\mathbf{Q})}{\frac{1}{N}\sum_{j=1}^{N} I_j(\mathbf{Q})} - 1, \quad (1)$$

where the sum is over all $N = 961$ images in the scan. In Fig. 1 A and B, we show an example of a diffraction image before and after this processing, i.e., $I_j(\mathbf{Q})$ and $\delta I_j(\mathbf{Q})$, respectively. In the processed image in Fig. 1B, the anisotropy shows up clearly as changing intensities with the azimuthal angle in the vicinity of the first and second diffraction rings. This means that the structure factor, $S(Q)$, of the illuminated sample volume (approximately 60 nm × 60 nm × 5 μm) is not isotropic, even though the sample appears completely amorphous (i.e., there is no sign of Bragg peaks). Fig. 1C shows more examples of the processed images $\delta I_j(\mathbf{Q})$. We can see that the pattern changes between images, implying that the anisotropic structure changes at different positions on the sample. We note in passing that, as argued in our previous work [9], these non-centrosymmetric patterns do not violate Friedel symmetry because of the relatively large diffraction angle (25° at the first ring); as will be shown below, the patterns become more centrosymmetric with the high-energy X-ray beam in the total scattering data. We also note that further characterizations of the anisotropy, including its dependence on beam size, its spatial distribution, the absence of X-ray radiation effects, etc., are reported in our previous work [9].

Curiously, despite changes in the amplitude and orientation of the anisotropy, most patterns appear to show similar features. For example, it appears that an increase in the intensity of the first diffraction peak (which shows up as red hues in these plots, e.g., in the lower left part of Fig. 1B) is usually accompanied by a movement of the second peak towards higher $Q \equiv |\mathbf{Q}|$ (which shows up as blue hues inside of the second ring and red outside). The opposite holds true as well: a decrease in the first peak intensity appears to be correlated with the second peak moving towards lower Q. To further quantify this observation, for the images shown in Fig. 1C, we choose azimuthal ranges with an opening angle of 20° where the deviation exceeds 2% on the first peak, i.e., where $\delta I(Q_{m1}) < -0.02$ or $\delta I(Q_{m1}) > 0.02$ with $Q_{m1} = 2.85\,\text{Å}^{-1}$ indicating the center of the first peak. These azimuthal slices are indicated by the dashed lines. We choose ±2% as the threshold in order to be well above the background level which may reach ~ ±1%. Then, we obtain $\delta I(Q)$ that is averaged over this azimuthal range, and normalize it to its value at the first peak, $\delta I(Q_{m1})$. The results are plotted in Fig. 1D, as transparent red if $\delta I(Q_{m1}) > 0.02$ and transparent blue if $\delta I(Q_{m1}) < -0.02$. The average of all the transparent red (blue) curves is shown as the solid red (blue) curve.

We can see in Fig. 1D that $\delta I(Q)$ in different images share very similar features, not only qualitatively concerning changes in the first and second rings as described above, but also quantitatively as demonstrated by the agreement between different curves of the same color. Except for fluctuations in the low-Q region which are caused by the low scattering signal from the sample and the high air scattering background, the positions and shapes of the maxima and minima appear to reproduce well between different curves. This suggests that the red and the blue curve each corresponds to a specific deviation from the average structure. Moreover, it appears that the two curves are very close to the

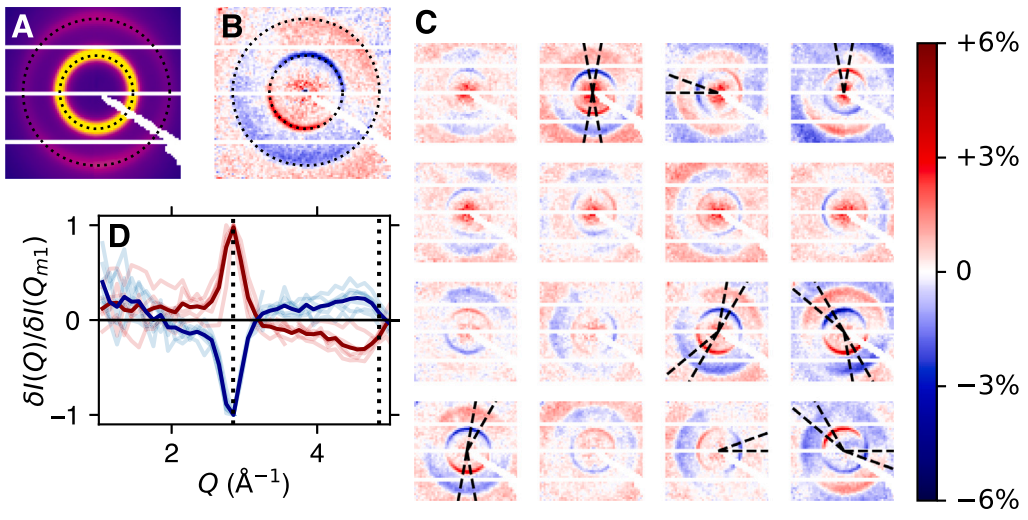

Fig. 1. Anisotropy analysis of the nano-diffraction data. (A) An example diffraction pattern $I_j(\mathbf{Q})$. The dotted rings indicate the maximum position of the first and second diffraction rings. The color scale is saturated to show the second diffraction ring more clearly. (B) The diffraction pattern in panel A after the processing, $\delta I_j(\mathbf{Q})$ (see text for details of the processing procedure). (C) Examples of processed images. Dashed lines indicate azimuthal ranges (with 20° opening angle) from which the $\delta I(Q)$ data is taken to make the plot in panel D. (D) Transparent red/blue lines show $\delta I(Q)$ from panel C normalized to their maxima at 2.85 Å^{-1}. The dark red/blue lines show the average. The vertical dotted lines indicate the Q position of the first and second maxima (i.e., the dotted rings in panels A-B). (For interpretation of the references to color in this figure legend, the reader is referred to the web version of this article.)

negative of each other, i.e., $[\delta I(Q)/\delta I(Q_{m1})]_{\text{red}} \approx -[\delta I(Q)/\delta I(Q_{m1})]_{\text{blue}}$. Therefore, the $I(Q)$ data at any given sample position and in any direction appears to be a linear combination of two distinct structures, one represented by the red curve and the other by the blue curve. For simplicity, in the following, we refer to the structural deviation corresponding to the red (blue) curve as the "H (L) pattern".

It is worth pointing out the implication of this observation, which goes significantly beyond the mere existence of anisotropy in the diffraction patterns. While the observation of anisotropy implies that the structure of this apparently amorphous sample is not the same in all directions, the structural deviation can in principle take many different forms. For example, there is no a priori reason why changes in the first peak intensity are correlated with the position of the second peak. Thus, the bimodality of the distribution is a significant observation which suggests the existence of two specific structural patterns, and that the average structure in any given direction may be interpreted as a mixture of these two with changing ratios. Note, however, that both patterns arise from the same group of atoms, so they actually describe the same 3-dimensional structure projected onto different directions.

To further demonstrate the bimodality of the structure, we analyze the total scattering data which covers a much larger Q-range up to more than 23 Å^{-1}. The processing procedure is the same as described above, except that the images are normalized by the summed intensity on the whole detector, which helps reduce the background at high Q where the elastic scattering intensity is low. A subset of the processed images is shown in Fig. 2A. Note that the color scale is limited to ±0.5% because the degree of anisotropy is largely reduced compared to the nano-diffraction data, which is very likely caused by the much larger beam size (about 25 times bigger in area). Nonetheless, clear traces of anisotropy still remain, and the direction of anisotropy changes with the position on the sample. More quantitatively, we repeat the procedure described above to obtain the anisotropic structures, with a threshold at ±0.2% for deviation in the first peak intensity, and the results are plotted in Fig. 2C. Despite the lower signal-to-noise ratio, the bimodality discussed above can be observed in this dataset as well. Moreover, the data overlays well with the nano-diffraction results, shown in Fig. 2C as dashed black lines, in the common Q-range up to about 5 Å^{-1}, despite being taken from different parts of the sample and with measurements performed using different X-ray instruments. This further confirms the bimodality of the diffraction pattern.

It can be seen in Fig. 2C that modulations in $I(Q)$ persist up to at least 10 Å^{-1}. The main features of the anisotropy can be compared with the azimuthally integrated scattering intensity, $I(Q)$, averaged over the dataset, which is shown in Fig. 2B. The center positions of the peaks are indicated by the vertical dashed lines. The following observations can be made for the H pattern (and the opposite is true for the L pattern): (1) The intensity of the first peak (around 2.8 Å^{-1}) increases. This is known to signify an increased degree of ordering in the intermediate range, starting from the third shell [12]. (2) The second peak (around 4.8 Å^{-1}) shifts slightly to higher Q, which shows up as $\delta I(Q) > 0$ on the high-Q side and $\delta I(Q) < 0$ on the low-Q side, while the other peaks do not seem to shift. This suggests a slight reduction in the average nearest-neighbor distance. (3) The shoulder of the second peak (around 5.6 Å^{-1}) becomes more intense. Since this shoulder appears in some other Pd-based metallic glasses as well and it has been attributed to icosahedral SRO [13,14], the observations here may suggest that icosahedral SRO is more enhanced in the H pattern. (4) The higher-order peaks appear to decrease slightly in intensity. These peaks are related to the SRO but the connection may be less direct; we will further discuss their implication in the Discussion section below.

Before proceeding, we note that a common suspicion given the observations, in particular the diffraction patterns shown in Fig. 1C and Fig. 2A, is chemical phase separation. However, while chemical phase separation might explain why the diffraction pattern would change at different sample positions, it cannot explain the anisotropy which concerns the structure of the exact same group of atoms, only in different directions. Moreover, in a phase-separated sample, one may expect the position of the first diffraction maximum to change depending on sample position, but no such change is observed [9]. In addition, chemical phase separation is expected to increase with annealing close to T_g, while the anisotropy is observed to vanish. In Fig. 2E-G, we further show EDX mappings of an arbitrary region on the sample, demonstrating that there are no detectable compositional inhomogeneities (the slightly elevated level of fluctuation observed in the Cu concentration is likely due to its low percentage). In particular, there is no structural motif corresponding to the distribution of anisotropies reported in our previous work (Ref. [9], Fig. S6). Therefore, chemical phase separation is excluded as the origin of the anisotropic diffraction patterns.

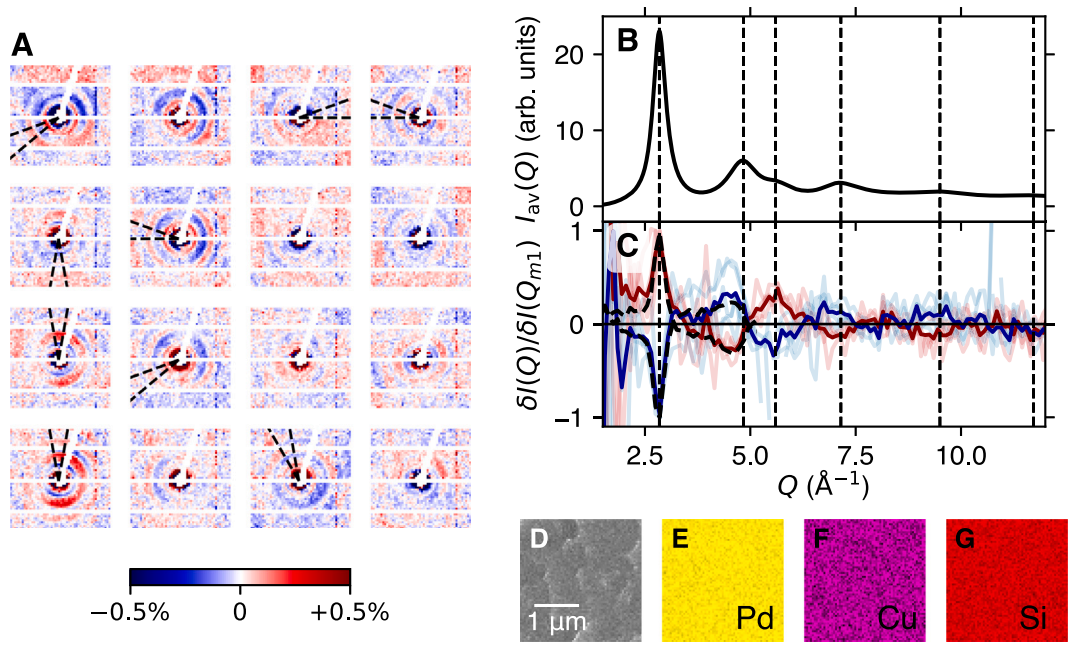

Fig. 2. Anisotropy analysis of the total scattering data. (A) Examples of processed images. Dashed lines indicate azimuthal ranges (with 20° opening angle) from which the $\delta I(Q)$ data is taken to make the plot in panel C. (B) Azimuthally integrated intensity $I(Q)$ averaged over all images. The dashed vertical lines indicate the positions of peaks. (C) Transparent red/blue lines show $\delta I(Q)$ from panel A normalized to their maxima at 2.85 Å^{-1}. The dark red/blue lines show the average. The dashed black curves show the result with nano-diffraction (i.e., the dark red/blue lines in Fig. 1D). (D) SEM image of an arbitrary area on the sample and the corresponding EDX mappings of (E) Pd, (F) Cu, and (G) Si. (For interpretation of the references to color in this figure legend, the reader is referred to the web version of this article.)

3.2. Anisotropic pair distribution functions

To better understand the structural anisotropy, we perform pair distribution function (PDF) analysis on the data using the software *PDFgetX3* [15]. First, we perform it on the average azimuthally integrated diffraction intensity shown in Fig. 2B. The results are shown in Fig. 3A, whose main features, including the peak positions, agree well with previous results on an alloy with a very similar composition ($Pd_{78}Cu_6Si_{16}$) at high temperatures [16].

Next, we examine in detail how the H and L patterns differ from the average structure, using the modulations $\delta I(Q)/\delta I(Q_{m1})$ reported in Fig. 2. We use the following procedure: (1) Multiply $\delta I(Q)/\delta I(Q_{m1})$ by 0.05, so that it matches the level observed in the nano-diffraction data. This is supported by the good agreement between the nano-diffraction and total scattering data shown in Fig. 2C, which suggests the possibility of reaching at least ±5% anisotropy on the first peak in $I(Q)$ with a small X-ray beam. Considering the 5 μm thickness of the sample, it is likely that some averaging effects already happened even with a nano-sized beam, so the observed ±5% level is probably a lower limit for the possible deviations of the H and L patterns from the average. (2) Truncate the data below 2 Å^{-1} and above 10 Å^{-1} in order to reduce noise. This is supported by the lack of significant features in $\delta I(Q)$ outside of the Q-range from 2 to 10 Å^{-1} in Fig. 2C. In addition, the intensity $I(Q)$ is low outside of this range, so small changes upon it do not give rise to much difference in the reconstructed PDF. (3) Calculate $I(Q)$ based on the above. Steps 1-3 above amount to using the following formula:

$$I_{H,L}(Q) = \begin{cases} I_{av}(Q)\left[1 + 0.05\frac{\delta I_{H,L}(Q)}{\delta I(Q_{m1})}\right], \\ \qquad (\text{for } 2\,\text{Å}^{-1} \le Q \le 10\,\text{Å}^{-1}) \\ I_{av}(Q), \quad (\text{otherwise}) \end{cases} \tag{2}$$

where $I_{av}(Q)$ is the average structure shown in Fig. 2B. (4) Then, we use *PDFgetX3* [15] to calculate $G_{H,L}(r)$ based on the intensities $I_{H,L}(Q)$. (5) Finally, we subtract from $G_{H,L}(r)$ the average PDF, $G_{av}(r)$ (shown in Fig. 3A), to obtain the differences $\Delta G_{H,L}(r) = G_{H,L}(r) - G_{av}(r)$ and plot them in Fig. 3B.

The differences $\Delta G_{H,L}(r)$ contain many interesting features that are worth discussing. Overall, the H and L patterns deviate from the average structure in almost exactly opposite ways, which is expected since $I_{H,L}(Q)$ deviate from the average in opposite ways as shown in Fig. 2C. The details of $\Delta G_{H,L}(r)$ vary for different peaks in $G_{av}(r)$ which are indicated by dashed vertical lines. For the H pattern, on the first peak, $\Delta G(r)$ is very close to zero at the peak center (2.8 Å), but $\Delta G_H(r)$ is positive on the low-r side, suggesting a slight shift to lower r of the 1st coordination shell. At the same time, there is increased intensity between the second and third peaks (centered at 4.6 Å and 5.4 Å, respectively), suggesting some loss of the intermediate-range structure corresponding to these two peaks. Starting from the fourth peak (centered at 7.0 Å), the oscillations in $\Delta G(r)$ appear in phase with those in $G_{av}(r)$, suggesting an increase in ordering in these higher-order coordination shells. The opposite is true for the L pattern: a slight shift to higher r at the first peak, an increase in the structural ordering corresponding to the second and third peaks, and a reduction in ordering starting from the fourth peak.

In order to better visualize these features, we enhance the differences $\Delta G_{H,L}(r)$ by a factor of 10, and plot in Fig. 3C: $G_{H,L}(r) = G_{av}(r) + 10\Delta G_{H,L}(r)$. Although this enhancement is artificial, done mainly for the purpose of demonstrating the trend of structural deviations, it is possible that such high levels of deviations may actually exist locally but are not observed because of averaging effects in the X-ray illuminated sample volume (at least 60 nm × 60 nm × 5 μm). The $G_{H,L}(r)$ thus obtained confirm the observations above: for the H pattern, the 1st coordination shell is significantly contracted, as shown in the inset; higher-order shells starting from the 4th are more ordered, with enhanced structural correlations, although the peak positions do not change; more interestingly, the second and third peaks almost appear to merge into a single one. Overall, this enhanced H pattern resembles that of a "simple" liquid such as liquid argon [17]. In the L pattern, on the other hand, the second and third peaks become sharper and more separated. However, this appears to be at the cost of an almost complete loss of structural correlations beyond the fourth peak (centered at 7.0 Å^{-1}), as well as a slight expansion of the 1st coordination shell as shown in the inset of Fig. 3C.

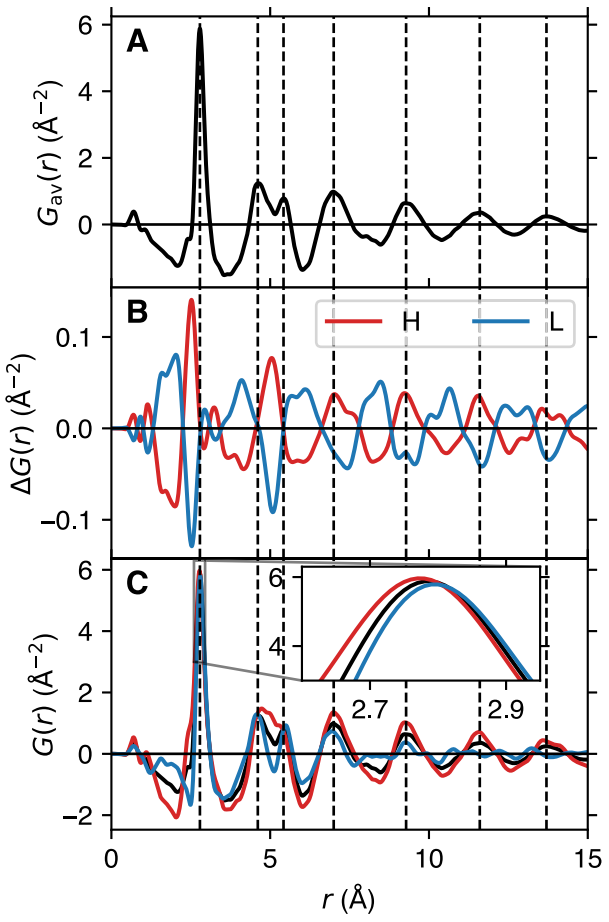

Fig. 3. The real-space anisotropic structure. (A) PDF of the average structure, $G_{av}(r)$. (B) Difference of the H (red) and L (blue) patterns from the average structure, assuming 5% change in intensity at the first peak of $I(Q)$ (at 2.85 Å^{-1}). (C) PDF augmenting the change in panel B by 10 times. The black line is the average structure shown in panel A. Inset shows the changes close to the first peak. (For interpretation of the references to color in this figure legend, the reader is referred to the web version of this article.)

We again emphasize that the two patterns originate from the same sample volume which is illuminated by the X-ray beam, so they describe the same structure in different directions and cannot be explained by inhomogeneities in the sample such as chemical phase separation. In our previous work [9], we have also been able to exclude many other alternative explanations by, for example, measuring the sample after annealing at increasing temperatures, and we conclude that the anisotropy must arise from the intrinsic structure of the sample. In the present work, using high-energy X-ray total scattering, we are able to reconstruct the anisotropic structure in real space, which provides crucial details of the atomic arrangements corresponding to the different directions. The significance of these observations will be further discussed in the Discussion session below.

3.3. Effects of annealing

To understand how the structure changes upon annealing, we perform PDF analysis on the sample which has been annealed at 629 K for 10 min and in which the anisotropy has been observed to disappear without crystallization [9]. In Fig. 4A, we plot as orange line the difference $G_{ann}(r) - G_{asdep}(r)$ augmented by a factor of 10 to ease comparison with the structure of the as-deposited sample (black line). For all peaks of $G_{asdep}(r)$, there is an increase (i.e., $G_{ann}(r) - G_{asdep}(r) > 0$) on the low-$r$ side, indicating a slight contraction in all the coordination shells. To further quantify this, we fit each peak of $G(r)$ with a Gaussian function on a constant background, in order to extract the peak center position. In the inset of Fig. 4A, we plot the ratio between the center positions of the annealed sample and those of the as-deposited sample. All of the ratios are below 1, confirming that there is a general contraction in the coordination shells. For higher coordination shells, the ratio is close to a constant level of 0.997, suggesting a volume contraction of approximately 0.9% (but note that the actual change in density may be slightly different due to structural rearrangements). This is comparable with the general behavior of metallic glasses under annealing [18].

Interestingly, however, the ratio between the first peaks of $G(r)$ is higher than 0.999, suggesting that the 1st coordination shell does not contract nearly as much. This curious contrast between the 1st coordination shell and the others, as evidenced in the inset of Fig. 4A, requires further investigation. Hence, we look into possible changes in the width of the first peak. Because this peak increases slightly in amplitude after annealing, it is expected to become slightly narrower as well, but this needs to be confirmed with an independent method to characterize the change in width. However, because the center position, amplitude, and width of the peak change at the same time, as indicated in the schematic diagram in the inset of Fig. 4B, it is difficult to directly compare the widths of the as-deposited and the annealed samples. Therefore, we use the following method, as illustrated in the inset: for each value of $G(r)$, we take a horizontal line-cut and extract the range Δr in which $G(r)$ is higher than this value. In Fig. 4B, we plot the difference between Δr of the two samples, $\Delta r_{ann} - \Delta r_{asdep}$, against the value of $G(r)$. It can be seen that the difference in Δr is negative for low values of $G(r)$, increases monotonically with $G(r)$, and becomes positive for $G(r) > 1.82$ Å^{-2}. This situation can be illustrated by the schematic diagram in the inset, which provides evidence that the peak becomes narrower after annealing. Note that this method is free from the influence of shifts in the peak position, since such shifts do not change the value of Δr.

Another way to compare the sharpness of the peaks is by calculating the second moment σ_r, defined here as $\sigma_r \equiv \int_{r_1}^{r_2}(r - r_m)^2 G(r)dr$, where r_1 and r_2 are the first zeros of $G(r)$ around the first peak and r_m is the peak center position. In this way, we obtain $\sigma = 0.1082$ Å and 0.1076 Å for the as-deposited and annealed samples, respectively. This provides further evidence that the first peak of $G(r)$ becomes sharper upon annealing.

The sharpening of the first peak of $G(r)$ suggests that, while the average nearest-neighbor distance changes very little, its distribution becomes narrower after annealing. This is consistent with the observation above that the anisotropic structure in the as-deposited sample has different average nearest-neighbor distances in different directions (see Fig. 3C) and the disappearance of anisotropy upon annealing observed previously [9]. In other words, our results suggest that annealing leads to atomic rearrangements so that the nearest-neighbor distances become more uniform. In addition, the contraction of higher coordination shells indicates that these rearrangements are correlated with, and possibly driven by, an enhancement in medium-range ordering and an overall densification.

One might ask how the structure after annealing compares with the anisotropic H and L structural patterns in the as-deposited sample. Since one of the main features of the anisotropic structure lies between the second and third peaks in $G(r)$, in Fig. 4C we focus on this r-range. While it is clear that both peaks shift towards low-r, the region between the peaks changes little, as can be inferred also from the difference $G_{ann}(r) - G_{asdep}(r)$ shown in Fig. 4A. Therefore, it appears that the annealed sample resembles neither the H nor the L pattern. This should not come as a surprise because, as emphasized above, the H and L patterns describe the projection of the same 3-dimensional structure and thus should not be considered as independent. The results above thus suggest that annealing destroys the anisotropic structure, i.e., the H and L patterns at the same time, leading to a more compact and isotropic structure.

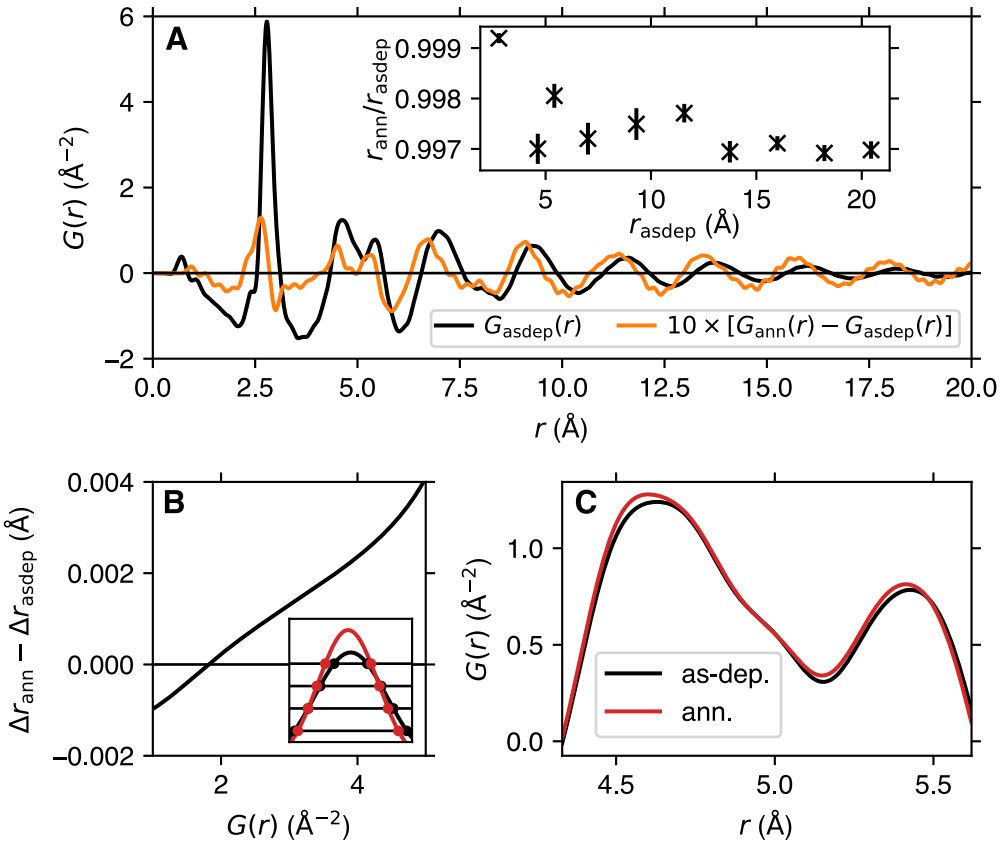

Fig. 4. Effects of annealing on the sample structure. (A) PDF for the as-deposited sample (black) and the change in the annealed sample augmented by a factor of 10 (orange). Inset shows the ratio between the peak center positions of the as-deposited and annealed samples. (B) Peak width difference as a function of $G(r)$ between the annealed and as-deposited samples (see text). Inset demonstrates the concept (not to scale): for the sharper peak, the width is narrower at lower $G(r)$ values, and it becomes broader at increasing values of $G(r)$. (C) Comparison between the samples focusing on the range around the second and third peaks. (For interpretation of the references to color in this figure legend, the reader is referred to the web version of this article.)

3.4. Calorimetric measurements

To better characterize the sample, we perform FDSC scans on small pieces cut from the sample. Each piece is placed onto the FDSC chip, and the following scan is performed at least twice in a row: the sample is first heated up to 723 K or 743 K at 500 K/s, then kept at that temperature for 0.1 s, and cooled down to 298 K at 500 K/s. The data is then corrected following the procedure proposed by Sonaglioni et al. [19]: in step 1, the symmetric line correction is used, and in step 2 a linear correction is applied to match the c_P values in the liquid and glass regimes from conventional differential scanning calorimetry (DSC) data [20] (black circles and dashed line in Fig. 5A). Note that the correction parameters in step 2 are calculated based on the second FDSC heating scan, and the same parameters are used to correct the first FDSC heating scan, thereby preserving all differences between these two scans. The red and blue curves in Fig. 5A show an example of the specific heat $c_P(T)$ from the first and second heating scans, respectively, after the correction procedure. With respect to conventional DSC, the enthalpy recovery peak shifts to high T, which is expected because of the much higher heating rate used here, compared with a rate of 0.33 K/s used in conventional DSC [20] (a similar degree of increase is seen in a previous work on Pd-based metallic glasses as well [21]). We have also examined the effects of annealing: in this case, the as-deposited sample is heated up to 629 K at 500 K/s, kept at 629 K for 10 min, and then cooled down at 500 K/s. Then, FDSC measurements are performed by heating to 743 K at 500 K/s, and the results are shown as the green curve in Fig. 5A. We can see that the enthalpy recovery peak is much more enhanced and shifted to even higher T, suggesting a significant increase in the kinetic stability of the sample after annealing. Similarly significant enhancements of this peak and shifts to higher temperatures after annealing close to T_g are seen in other works on metallic glasses as well [22,23], although an alternative explanation for the increased temperature is given below in the Discussion section. We note that no sign of crystallization is observed during any of the scans in the present work.

The difference between the first and second FDSC heating scans is worth further investigation. Comparing the curves in Fig. 5, the most noticeable change is in the enthalpy recovery peak, which sees a clear enhancement in the second heating. In order to see more subtle changes, we subtract the first from the second heating scan and obtain the difference, $\Delta c_P(T)$. This is repeated for three different pieces from the as-deposited sample, and in Fig. 5B we plot the average (black curve) as well as the minimum-maximum range (shaded region) of the results. It can be seen that, in addition to the lower enthalpy recovery peak, showing up as $\Delta c_P < 0$ in the region around 700 K, there is also a broader endothermic peak ($\Delta c_P > 0$), starting at around 500 K and peaked around 615 K. This is reminiscent of the "shadow glass transition" reported in some glasses quenched at high rates [24,25]. Since the signal is small, to further validate it, we perform the same scans on a ribbon sample of the same nominal composition, $Pd_{77.5}Cu_6Si_{16.5}$. The results are shown as purple lines in Fig. 5B. The noise level is lower because the ribbon sample is much thicker (about 45 μm) and hence the pieces have a higher mass, but the endothermic peak is clearly absent. This provides evidence that the endothermic peak in the vapor-deposited sample is a real signal.

Due to the presence of this broad endothermic peak, the enthalpy of the as-deposited glass is not as high as suggested by its relatively low enthalpy recovery peak seen in Fig. 5A. For a more quantitative description, we calculate the enthalpy difference, $\Delta H(T)$, by integrating

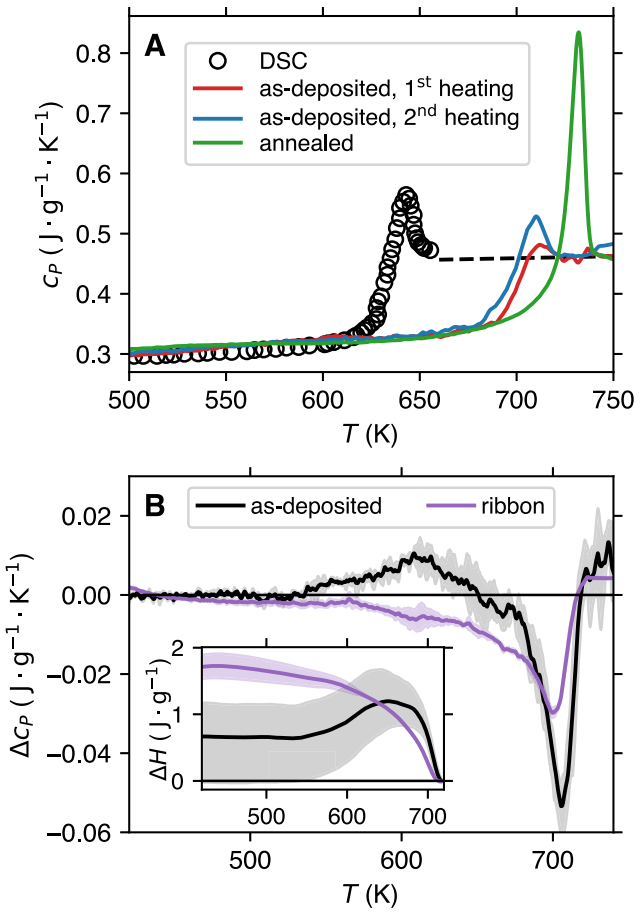

Fig. 5. FDSC results. (A) The red and blue lines show c_P obtained from the first and second heating scans of the as-deposited sample with FDSC, respectively. The green line shows the first heating scan after annealing the sample at 629 K for 10 min. The black circles show conventional DSC data from Ref. [20] on a bulk metallic glass sample of the same nominal composition, while the black dashed line shows a linear extrapolation from the liquid region in Ref. [20]. (B) Difference between the first and second heating scans of the as-deposited sample (black line) and a melt-spun ribbon sample of the same nominal composition (purple line). The lines show the average of different scans, and the transparent shaded regions indicate the range of minimum-maximum among different samples. Inset shows the enthalpy difference integrated from 720 K (in the supercooled liquid region) to below. (For interpretation of the references to color in this figure legend, the reader is referred to the web version of this article.)

Δc_P from 720 K (in the supercooled liquid region):

$$\Delta H(T) = -\int_{T}^{720\,\mathrm{K}} \Delta c_P(\tau)\, d\tau. \tag{3}$$

The results are shown in the inset of Fig. 5B. Since during the first scan, the sample is heated to above the enthalpy recovery peak, kept there for at least 0.1 s, and cooled down at 500 K/s, the thermodynamic state prior to the second heating is a well-defined one, namely that of a glass quenched from the supercooled liquid state at 500 K/s. Therefore, $\Delta H(T)$ can be understood as the difference in enthalpy between the original sample (as-deposited or melt-spun) and a $Pd_{77.5}Cu_6Si_{16.5}$ glass quenched at 500 K/s. We can see that, at low temperatures, ΔH for the vapor-deposited sample is closer to 0 than at higher temperatures. In comparison, ΔH for the ribbon sample approaches a constant high value at lower temperatures, which is expected given that the effective quenching rate for the ribbon sample is much higher than 500 K/s [24,26]. The behavior of the as-deposited sample, on the other hand, is more curious. The calculated ΔH at low temperatures appears to indicate that the as-deposited sample is thermodynamically more stable than the ribbon sample but somewhat less stable than the glass prepared at a cooling rate of 500 K/s. However, due to the sub-T_g endothermic peak, the data also seems to suggest that upon heating, the sample needs to absorb heat before relaxation at higher temperatures.

Remarkably, an extra sub-T_g endothermic process and a reduced enthalpy recovery peak has been observed in a $La_{55}Al_{25}Ni_{20}$ metallic glass that first went through plastic deformation and was then annealed much below T_g [27]. In addition, the authors find that, after sufficient sub-T_g annealing, the enthalpy difference arising from the sub-T_g endotherm may compensate for the reduction in the enthalpy recovery peak, leading to two states that are enthalpically close but structurally different, similar to the present case (cf. Fig. 5B). This is explained by the heterogeneity within the sample, which contains regions with high enthalpy that relax slowly (hence the reduced enthalpy recovery peak) as well as regions that relax readily upon annealing (hence the sub-T_g endotherm). This is applicable to our sample as well, where the elevated substrate temperature during deposition may have played the role of sub-T_g annealing. How this may be related to the long-range anisotropy will be further discussed in the next section.

4. Discussion

The observation of long-range structural anisotropy suggests not only the existence of anisotropic local structural units, but also the alignment of these units with long-range correlations. The existence of local ordering in glasses that extends beyond nearest neighbors, often referred to as medium-range ordering, is well-established nowadays [2,3], and the ordered unit is often anisotropic [28,29] (not surprisingly given that a large number of atoms are needed to reach true isotropy). Perhaps less expected is the implication that these local units can find a way to align with each other even at mesoscopic scales, up to tens of nanometers and beyond, in a sample that appears completely amorphous. However, long-range alignment of anisotropic units is not a rare phenomenon in non-crystalline materials, as it is seen, for example, in the nematic phase of liquid crystals. Moreover, in a recent study on vapor-deposited molecular glasses, orientationally ordered domains are indeed found to exist on the mesoscopic scale from tens to hundreds of nanometers [30]. Therefore, our results suggest that similar phenomena may happen for metallic glasses as well. The main difference is that in organic glasses, the constituent molecules often have a highly anisotropic shape (for example, disk-like in Ref. [30]), while metallic glasses are traditionally thought of as atomic, thus lacking intrinsic anisotropy. Hence, the results above bear the significant implication that locally ordered units may be important for the structure of metallic glasses as well.

The results in Fig. 3C provide additional clues on the details of the anisotropic structure. They suggest that, in this structure, in a certain direction there is an increased likelihood of atomic pairs with distances around 5 Å, between the 2nd and 3rd peaks of $G(r)$, while this likelihood decreases in another direction. These two directions are likely orthogonal to each other within the local structure, given the high frequency of dipolar patterns observed in Fig. 1C. The origin of the 2nd and 3rd peaks of $G(r)$, which are often viewed in the literature as a split second peak [31,32], has been under discussion for many years. Simulation results have provided evidence that this peak splitting in densely packed glasses, and the lack thereof in the liquid state, originates from the relatively low ratio of two-atom-shared connections (i.e., the Voronoi polyhedra around the pair of atoms have exactly two atoms in common) with respect to one- and three-atom-shared connections, and this ratio increases as the system is heated up into its liquid state [32]. From this viewpoint, our results would suggest that there is an increase of two-atom-shared connections in the direction of the H pattern, and a decrease thereof in the direction of the L pattern. Alternatively, it should be noted that trigonal prisms have been proposed as the basic structural units for metal–metalloid glasses in general [33] and for Pd-Cu-Si alloys in particular [16,34]. These units are intrinsically anisotropic, and if there is a tendency for them to align, it would give rise to an anisotropic overall structure. In particular, in

the plane parallel to the trigonal base, the $G(r)$ would show a split second peak, similar to 2-dimensional hard disk system [35]. This would be consistent with the slightly larger nearest-neighbor distance in this direction, as the trigonal base consists only of Pd atoms which have the largest atomic radius among the constituent atoms. These hypotheses may be tested in future works.

Notably, anisotropy has been widely observed in vapor-deposited organic glasses [36]. In most cases, the anisotropy is global, which results from the symmetry breaking between in- and out-of-plane directions during the deposition process [37], although as mentioned above, a recent work has found mesosopic local ordering as well [30]. In general, the anisotropy is found to disappear upon annealing above the glass transition temperature, T_g [38], similar to the present case. Since the as-deposited glass is found to exhibit higher kinetic stability and lower enthalpy [36], the disappearance of anisotropy is connected with the loss of stability. It should be noted, however, that the as-deposited glass can be isotropic as well with a high level of stability [36,39], so the presence of anisotropy is not necessarily a sign of higher stability.

For metallic glasses, earlier works have found evidence for global anisotropy between in- and out-of-plane directions in vapor-deposited ferromagnetic alloys, and it gets erased upon annealing [4–7], but our observation of local structural anisotropy between different in-plane directions [9] was the first such report to our knowledge. Another major difference is that the global structural anisotropy in the vapor-deposited ferromagnetic films shows up in scattering measurements as a shift in the first diffraction peak position [4], while we see no observable change in the first peak position between in- and out-of-plane directions [9].

Nonetheless, the results in earlier works may inform us on the possible physical mechanism behind our observations. In particular, Hellman [40] proposed a surface two-level model to describe the increase of anisotropy with elevated substrate temperatures during deposition, while the gradual decrease of anisotropy upon annealing is found to be consistent with a two-level model applicable to the bulk material [41]. In light of this, our observations may be explained as follows: taking into account that our sample is vapor-deposited while keeping the substrate at elevated temperatures ($0.80T_g$ to $0.85T_g$) [9], the large degree of anisotropy may have arisen from surface energy minimization. However, this anisotropic state is not preferred in the bulk material, possibly due to a lower density as suggested by our results in Fig. 4. Therefore, with annealing at increasing temperatures [9], more of the anisotropic states are able to jump over the energy barrier and reach a denser and more isotropic state that is preferred in the bulk material.

However, we again point out the major difference between our present results, where the anisotropy is local and is between different in-plane directions, and those by Hellman [40], where the anisotropy is global and arises directly from the symmetry breaking at the sample surface during deposition. The link between surface energy minimization and local in-plane anisotropy is perhaps not intuitive and needs further investigation. We speculate that the locally favored structural units during surface energy minimization have high in-plane anisotropy as well, and that there is a mechanism for these units to become aligned in a direction that is not in-plane or parallel to the surface normal, for example due to patterning by the substrate or due to the tilt angle during the deposition. Another possible mechanism for the alignment of anisotropic units is the existence of Eshelby inclusions [42,43], which carry with them strain fields that are anisotropic (quadrupolar) and can have long-range orientational correlations. In any case, since locally ordered units are a common feature among amorphous solids, our results suggest that in-plane structural anisotropy may exist in many other vapor-deposited glasses as well, including the ferromagnetic ones mentioned above; indeed, there is some evidence for it from small-angle neutron scattering measurements [44]. Therefore, we expect that more discoveries similar to those in the present study will be made in future works taking advantage of recent advancements in X-ray sources and nano-focusing capabilities.

Finally, we discuss possible thermodynamic scenarios for the sample based on the main observations above, which can be summarized as the following: (1) There is a high level of anisotropy in the as-deposited sample, which suggests a large degree of structural ordering. This is consistent with the recent simulation results by Leoni et al. [45] on a model vapor-deposited metallic glass, where enhanced ordering is observed when the substrate temperature is kept roughly in the range $0.85T_g$ to T_g, consistent with the condition in which our sample has been prepared. (2) Upon annealing close to T_g, higher-order coordination shells (4th and above) contract, which suggests densification. While this may seem contradictory to observation 1 above, we note that a recent work by Lou et al. [46] on a $Zr_{35}Cu_{47.5}Ag_{17.5}$ bulk metallic glass has indeed shown evidence for densification upon annealing which is accompanied by disordering. The authors interpret this as a liquid-liquid phase transition between a low-density structure in the as-cast sample with higher medium-range ordering (MRO) and a high-density structure with lower MRO. In light of this interpretation, we may identify the anisotropic structure observed in our as-deposited sample as the more ordered but less dense MRO structure, which gets destroyed when the sample is annealed close to T_g. We point out, however, that the structural changes observed in the present work happen in the SRO (the 1st coordination shell) as well.

A similar interpretation may be borrowed from a very recent work by da Silva Pinto et al. [47] where the authors studied a $Pd_{40}Ni_{40}P_{20}$ bulk metallic glass and found evidence for a transition between two MRO structures, MRO I and MRO II, when the as-cast sample was annealed at $0.96T_g$. Interestingly, after annealing the as-cast sample at $0.81T_g$, the authors observed the development of a sub-T_g peak in the calorimetric trace. This is similar to our observation of an extra sub-T_g peak in the FDSC scan of the as-deposited sample (see Fig. 5). This is consistent with the results of da Silva Pinto et al. since our sample was deposited at elevated substrate temperatures, hence having sub-T_g annealing effects already during the deposition. In addition, da Silva Pinto et al. observe the development of a super-T_g peak upon annealing at $0.96T_g$, which could explain the significant increase in the apparent T_g upon annealing (see Fig. 5A). However, in another work [48], this super-T_g peak was not found for $Pd_{40}Ni_{40}P_{20}$, showing that further investigation needs to be done for a clear and comprehensive understanding of these systems. In the present case, because the sample can change significantly in shape when heated far above T_g, the FDSC data becomes particularly noisy at high temperatures, preventing conclusions about the existence of a possible super-T_g peak. The detailed characterization of the thermodynamic state of this family of Pd-based metallic glasses can be the focus of future works.

Given the available observations and considering the results from recent works on metallic glasses [46–48] mentioned above, we may speculate the thermodynamic state of the sample as follows: After deposition at a substrate temperature between $0.80T_g$ and $0.85T_g$, the sample is in a highly ordered and anisotropic state with a predominant local state S1. This S1 state may be characterized, in two different (likely orthogonal) directions, by the H and L patterns shown in Fig. 3, and it has a relatively low density. When heated up, the sample (S1 state) absorbs heat, leading to the apparent sub-T_g endotherm, after which it gains enough degrees of freedom to reach another state, S2, that is more dense and has a more uniform distribution of nearest-neighbor distances. In the meantime, the sample loses its anisotropy on the mesoscopic scale. It should be noted, however, that the sample appears completely amorphous in all cases and always contains a distribution of local structures. Therefore, S1 and S2 refer to overall structural motifs, and the transition between them is not expected to be as sharp as the one between different crystalline phases. Note that this description does not exclude the existence of the S2 local state already in the as-deposited sample, i.e., that the as-deposited sample is heterogeneous and contains a mixture of S1 and S2 states. This would

be consistent with the interpretation of a La-based metallic glass sample with similar thermodynamic behaviors [27], as mentioned above. In this case, the observation of a significant level of anisotropy in the as-deposited sample (more than ±5% on the first peak with nano-diffraction) would suggest that a large fraction of the sample is in the S1 state—a hypothesis to be tested in further studies. Nevertheless, our results point out the inadequacy of the tradition view of glasses as a single disordered state.

5. Conclusions

Using X-ray diffraction measurements with a small focus, we have observed long-range structural anisotropy in a $Pd_{77.5}Cu_6Si_{16.5}$ metallic glass sample made with vapor-deposition at elevated substrate temperatures. The anisotropic structure factor $S(Q)$ appears to follow a bimodal distribution with two well-defined patterns which we label as H and L, and they should correspond to two different directions in the local anisotropic structural units. The X-ray total scattering data further allows us to retrieve the pair distribution function $G(r)$ of the H and L patterns and find out that the H pattern has lower average atomic spacing and enhanced long-range correlations, while the L pattern is characterized by an enhanced splitting of the 2nd and 3rd peaks in $G(r)$. Upon annealing close to T_g, the anisotropy disappears and higher-order (4th and above) coordination shells contract, while the 1st shell becomes slightly sharper but mostly retains its center position. We interpret this as the destruction of the anisotropic local structure (S1) whose average spacing varies in different directions, to allow for a more compact and isotropic overall structure (S2). The FDSC results suggest that this is a two-step process, in which the S1 local state first absorbs heat and gains enough degrees of freedom similar to a glass transition, before relaxing to the S2 state. We expect that such local anisotropy and the associated structural and thermodynamic transitions are not limited to the present sample, and future works utilizing the newly available X-ray nano-focusing capabilities may discover similar phenomena in a larger family of amorphous systems.

CRediT authorship contribution statement

Peihao Sun: Writing – review & editing, Writing – original draft, Project administration, Methodology, Investigation, Funding acquisition, Formal analysis, Data curation, Conceptualization. **Alessandro Martinelli:** Writing – review & editing, Investigation, Data curation. **Jacopo Baglioni:** Writing – review & editing, Investigation, Data curation. **Francesco Dallari:** Writing – review & editing, Investigation, Data curation. **Marco Di Michiel:** Writing – review & editing, Writing – original draft, Methodology, Investigation, Data curation. **Alexey P. Melnikov:** Writing – review & editing, Investigation, Data curation. **Konrad Samwer:** Writing – review & editing, Investigation. **J.B. Hastings:** Writing – review & editing, Methodology, Investigation, Data curation. **Giulio Monaco:** Writing – review & editing, Writing – original draft, Supervision, Resources, Project administration, Methodology, Investigation, Data curation.

Declaration of competing interest

The authors declare that they have no known competing financial interests or personal relationships that could have appeared to influence the work reported in this paper.

Acknowledgments

The authors declare no competing interests. We acknowledge the ESRF for provision of synchrotron radiation facilities and we would like to thank Dr. Manfred Burghammer for assistance and support in using beamline ID13. We also thank Dr. Carlo Scian for technical support in the SEM and EDX measurements. This project has received funding from the European Union's Horizon 2020 research and innovation programme under the Marie Skłodowska-Curie grant agreement No. 101023787.

Appendix A. Supplementary data

Supplementary material related to this article can be found online at https://doi.org/10.1016/j.actamat.2025.120711.

References

[1] H.W. Sheng, W.K. Luo, F.M. Alamgir, J.M. Bai, E. Ma, Atomic packing and short-to-medium-range order in metallic glasses, Nature 439 (7075) (2006) 419–425, http://dx.doi.org/10.1038/nature04421.

[2] Y. Cheng, E. Ma, Atomic-level structure and structure–property relationship in metallic glasses, Prog. Mater. Sci. 56 (4) (2011) 379–473, http://dx.doi.org/10.1016/j.pmatsci.2010.12.002.

[3] S. Hilke, H. Rösner, G. Wilde, The role of minor alloying in the plasticity of bulk metallic glasses, Scr. Mater. 188 (2020) 50–53, http://dx.doi.org/10.1016/j.scriptamat.2020.06.070.

[4] X. Yan, M. Hirscher, T. Egami, E.E. Marinero, Direct observation of anelastic bond-orientational anisotropy in amorphous $Tb_{26}Fe_{62}Co_{12}$ thin films by x-ray diffraction, Phys. Rev. B 43 (1991) 9300–9303, http://dx.doi.org/10.1103/PhysRevB.43.9300.

[5] F. Hellman, E.M. Gyorgy, Growth-induced magnetic anisotropy in amorphous Tb-Fe, Phys. Rev. Lett. 68 (1992) 1391–1394, http://dx.doi.org/10.1103/PhysRevLett.68.1391.

[6] V.G. Harris, K.D. Aylesworth, B.N. Das, W.T. Elam, N.C. Koon, Structural origins of magnetic anisotropy in sputtered amorphous Tb-Fe films, Phys. Rev. Lett. 69 (13) (1992) 1939–1942, http://dx.doi.org/10.1103/PhysRevLett.69.1939.

[7] T.C. Hufnagel, S. Brennan, P. Zschack, B.M. Clemens, Structural anisotropy in amorphous Fe-Tb thin films, Phys. Rev. B 53 (18) (1996) 12024–12030, http://dx.doi.org/10.1103/PhysRevB.53.12024.

[8] Q. Zeng, H. Sheng, Y. Ding, L. Wang, W. Yang, J.-Z. Jiang, W.L. Mao, H.-K. Mao, Long-range topological order in metallic glass, Science 332 (6036) (2011) 1404–1406, http://dx.doi.org/10.1126/science.1200324.

[9] P. Sun, A. Martinelli, A.P. Melnikov, M. Burghammer, J. Antonowicz, R. Sobierajski, P. Fuoss, A.Q. Baron, K. Tamasaku, H. Ohsumi, F. Caporaletti, J.-P. Suuronen, R. Tucoulou, K. Samwer, J. Hastings, G. Monaco, Observation of long-range anisotropy in a vapor-deposited metallic glass, Materialia 30 (2023) 101847, http://dx.doi.org/10.1016/j.mtla.2023.101847.

[10] G.B.M. Vaughan, R. Baker, R. Barret, J. Bonnefoy, T. Buslaps, S. Checchia, D. Duran, F. Fihman, P. Got, J. Kieffer, S.A.J. Kimber, K. Martel, C. Morawe, D. Mottin, E. Papillon, S. Petitdemange, A. Vamvakeros, J.-P. Vieux, M. Di Michiel, ID15A at the ESRF – a beamline for high speed *operando* X-ray diffraction, diffraction tomography and total scattering, J. Synchrotron Radiat. 27 (2) (2020) 515–528, http://dx.doi.org/10.1107/S1600577519016813.

[11] H.-B. Yu, Y. Luo, K. Samwer, Ultrastable metallic glass, Adv. Mater. 25 (2013) 5904–5908, http://dx.doi.org/10.1002/adma.201302700.

[12] G.S. Cargill, Structure of metallic alloy glasses, in: H. Ehrenreich, F. Seitz, D. Turnbull (Eds.), in: Solid State Physics, vol. 30, Academic Press, 1975, pp. 227–320, http://dx.doi.org/10.1016/S0081-1947(08)60337-9.

[13] O. Gross, N. Neuber, A. Kuball, B. Bochtler, S. Hechler, M. Frey, R. Busch, Signatures of structural differences in Pt–P- and Pd–P-based bulk glass-forming liquids, Commun. Phys. 2 (2019) 83, http://dx.doi.org/10.1038/s42005-019-0180-2.

[14] K.F. Kelton, G.W. Lee, A.K. Gangopadhyay, R.W. Hyers, T.J. Rathz, J.R. Rogers, M.B. Robinson, D.S. Robinson, First X-Ray scattering studies on electrostatically levitated metallic liquids: Demonstrated influence of local icosahedral order on the nucleation barrier, Phys. Rev. Lett. 90 (2003) 195504, http://dx.doi.org/10.1103/PhysRevLett.90.195504.

[15] P. Juhás, T. Davis, C.L. Farrow, S.J.L. Billinge, *PDFgetX3*: a rapid and highly automatable program for processing powder diffraction data into total scattering pair distribution functions, J. Appl. Crystallogr. 46 (2) (2013) 560–566, http://dx.doi.org/10.1107/S0021889813005190.

[16] G.Q. Yue, Y. Zhang, Y. Sun, B. Shen, F. Dong, Z.Y. Wang, R.J. Zhang, Y.X. Zheng, M.J. Kramer, S.Y. Wang, C.Z. Wang, K.M. Ho, L.Y. Chen, Local structure order in $Pd_{78}Cu_6Si_{16}$ liquid, Sci. Rep. 5 (2015) 8277, http://dx.doi.org/10.1038/srep08277.

[17] J.L. Yarnell, M.J. Katz, R.G. Wenzel, S.H. Koenig, Structure factor and radial distribution function for liquid argon at 85 °K, Phys. Rev. A 7 (1973) 2130–2144, http://dx.doi.org/10.1103/PhysRevA.7.2130.

[18] H.S. Chen, The influence of structural relaxation on the density and Young's modulus of metallic glasses, J. Appl. Phys. 49 (1978) 3289–3291, http://dx.doi.org/10.1063/1.325279.

[19] D. Sonaglioni, E. Tombari, S. Capaccioli, Fast differential scanning calorimetry: new solutions in data treatment and applications to molecular glass-formers, Thermochim. Acta 719 (2023) 179385, http://dx.doi.org/10.1016/j.tca.2022.179385.

[20] G. Wilde, I.R. Lu, R. Willnecker, Fragility, thermodynamic properties, and thermal stability of Pd-rich glass forming liquids, Mater. Sci. Eng. A 375–377 (2004) 417–421, http://dx.doi.org/10.1016/j.msea.2003.10.218.

[21] M. Gao, J.H. Perepezko, Separating β relaxation from α relaxation in fragile metallic glasses based on ultrafast flash differential scanning calorimetry, Phys. Rev. Mater. 4 (2020) 025602, http://dx.doi.org/10.1103/PhysRevMaterials.4.025602.

[22] W.H. Wang, R.J. Wang, W.T. Yang, B.C. Wei, P. Wen, D.Q. Zhao, M.X. Pan, Stability of ZrTiCuNiBe bulk metallic glass upon isothermal annealing near the glass transition temperature, J. Mater. Res. 17 (2002) 1385–1389, http://dx.doi.org/10.1557/JMR.2002.0206.

[23] J. Wang, Y. Shen, J. Perepezko, M. Ediger, Increasing the kinetic stability of bulk metallic glasses, Acta Mater. 104 (2016) 25–32, http://dx.doi.org/10.1016/j.actamat.2015.11.048.

[24] Q. Yang, S.-X. Peng, Z. Wang, H.-B. Yu, Shadow glass transition as a thermodynamic signature of β relaxation in hyper-quenched metallic glasses, Natl. Sci. Rev. 7 (2020) 1896–1905, http://dx.doi.org/10.1093/nsr/nwaa100.

[25] Y. Yue, C.A. Angell, Clarifying the glass-transition behaviour of water by comparison with hyperquenched inorganic glasses, Nature 427 (2004) 717–720, http://dx.doi.org/10.1038/nature02295.

[26] Y.H. Liu, T. Fujita, D.P.B. Aji, M. Matsuura, M.W. Chen, Structural origins of johari-goldstein relaxation in a metallic glass, Nature Commun. 5 (2014) 3238, http://dx.doi.org/10.1038/ncomms4238.

[27] C. Meylan, J. Orava, A. Greer, Rejuvenation through plastic deformation of a La-based metallic glass measured by fast-scanning calorimetry, J. Non-Cryst. Solids: X 8 (2020) 100051, http://dx.doi.org/10.1016/j.nocx.2020.100051.

[28] A. Hirata, P. Guan, T. Fujita, Y. Hirotsu, A. Inoue, A.R. Yavari, T. Sakurai, M. Chen, Direct observation of local atomic order in a metallic glass, Nature Mater. 10 (2011) 28–33, http://dx.doi.org/10.1038/nmat2897.

[29] A. Hirata, L.J. Kang, T. Fujita, B. Klumov, K. Matsue, M. Kotani, A.R. Yavari, M.W. Chen, Geometric frustration of icosahedron in metallic glasses, Science 341 (2013) 376–379, http://dx.doi.org/10.1126/science.1232450.

[30] D. Chatterjee, S. Huang, K. Gu, J. Ju, J. Yu, H. Bock, L. Yu, M.D. Ediger, P.M. Voyles, Using 4D STEM to probe mesoscale order in molecular glass films prepared by physical vapor deposition, Nano Lett. 23 (2023) 2009–2015, http://dx.doi.org/10.1021/acs.nanolett.3c00197.

[31] C.H. Bennett, Serially Deposited Amorphous Aggregates of Hard Spheres, J. Appl. Phys. 43 (6) (1972) 2727–2734, http://dx.doi.org/10.1063/1.1661585.

[32] S.P. Pan, J.Y. Qin, W.M. Wang, T.K. Gu, Origin of splitting of the second peak in the pair-distribution function for metallic glasses, Phys. Rev. B 84 (2011) 092201, http://dx.doi.org/10.1103/PhysRevB.84.092201.

[33] P.H. Gaskell, A new structural model for transition metal–metalloid glasses, Nature 276 (1978) 484–485, http://dx.doi.org/10.1038/276484a0.

[34] S. Kajita, S. Kohara, Y. Onodera, T. Fukunaga, E. Matsubara, Structural analysis of Pd-Cu-Si metallic glassy alloy thin films with varying glass transition temperature, Mater. Trans. 52 (7) (2011) 1349–1355, http://dx.doi.org/10.2320/matertrans.M2011023.

[35] A. Huerta, D. Henderson, A. Trokhymchuk, Freezing of two-dimensional hard disks, Phys. Rev. E 74 (2006) 061106, http://dx.doi.org/10.1103/PhysRevE.74.061106.

[36] M.D. Ediger, Perspective: Highly stable vapor-deposited glasses, J. Chem. Phys. 147 (21) (2017) 210901.

[37] P. Luo, Z. Fakhraai, Surface-mediated formation of stable glasses, Annu. Rev. Phys. Chem. 74 (2023) 361–389, http://dx.doi.org/10.1146/annurev-physchem-042018-052708.

[38] K.J. Dawson, L. Zhu, L. Yu, M.D. Ediger, Anisotropic structure and transformation kinetics of vapor-deposited indomethacin glasses, J. Phys. Chem. B 115 (3) (2011) 455–463, http://dx.doi.org/10.1021/jp1092916.

[39] P. Luo, S.E. Wolf, S. Govind, R.B. Stephens, D.H. Kim, C.Y. Chen, T. Nguyen, P. Wąsik, M. Zhernenkov, B. Mcclimon, Z. Fakhraai, High-density stable glasses formed on soft substrates, Nature Mater. 23 (2024) 688–694, http://dx.doi.org/10.1038/s41563-024-01828-w.

[40] F. Hellman, Surface-induced ordering: A model for vapor-deposition growth of amorphous materials, Appl. Phys. Lett. 64 (15) (1994) 1947–1949, http://dx.doi.org/10.1063/1.111751.

[41] G. Hygate, M.R.J. Gibbs, Structural relaxation in metallic glasses: reversible and irreversible changes in a two-level systems model, J. Phys. F: Met. Phys. 17 (4) (1987) 815, http://dx.doi.org/10.1088/0305-4608/17/4/009.

[42] J.D. Eshelby, The determination of the elastic field of an ellipsoidal inclusion, and related problems, Proc. R. Soc. Lond. Ser. A. Math. Phys. Sci. 241 (1957) 376–396, http://dx.doi.org/10.1098/rspa.1957.0133.

[43] R. Dasgupta, H.G.E. Hentschel, I. Procaccia, Microscopic mechanism of shear bands in amorphous solids, Phys. Rev. Lett. 109 (2012) 255502, http://dx.doi.org/10.1103/PhysRevLett.109.255502.

[44] F. Hellman, A.L. Shapiro, E.N. Abarra, R.A. Robinson, R.P. Hjelm, P.A. Seeger, J.J. Rhyne, J.I. Suzuki, Long ferromagnetic correlation length in amorphous $TbFe_2$, Phys. Rev. B 59 (1999) 11408–11417, http://dx.doi.org/10.1103/PhysRevB.59.11408.

[45] F. Leoni, F. Martelli, C.P. Royall, J. Russo, Structural signatures of ultrastability in a deposited glassformer, Phys. Rev. Lett. 130 (2023) 198201, http://dx.doi.org/10.1103/PhysRevLett.130.198201.

[46] Y. Lou, S. Liu, J. Ge, H. Ying, S. Fu, W. Zhang, W. Dong, Z. Wu, X.-L. Wang, E.P. Gilbert, Y. Ren, S. Lan, An anomalous structure disordering in Zr–Cu–Ag supercooled glass-forming liquids, Intermetallics 159 (2023) 107930, http://dx.doi.org/10.1016/j.intermet.2023.107930.

[47] M.W. da Silva Pinto, L. Daum, H. Rösner, G. Wilde, Correlations between shadow glass transition, enthalpy recovery and medium range order in a $Pd_{40}Ni_{40}P_{20}$ bulk metallic glass, Acta Mater. (2024) 120034, http://dx.doi.org/10.1016/j.actamat.2024.120034.

[48] J. Shen, Y. Sun, J. Orava, H. Bai, W. Wang, Liquid-to-liquid transition around the glass-transition temperature in a glass-forming metallic liquid, Acta Mater. 225 (2022) 117588, http://dx.doi.org/10.1016/j.actamat.2021.117588.